Journal of Power Sources 266 (2014) 66–78

Contents lists available at ScienceDirect

Journal of Power Sources

journal homepage: www.elsevier.com/locate/jpowsour

Carbon corrosion of proton exchange membrane fuel cell catalyst layers studied by scanning transmission X-ray microscopy

Adam P. Hitchcock [a,*], Viatcheslav Berejnov [a], Vincent Lee [a], Marcia West [b], Vesna Colbow [c], Monica Dutta [c], Silvia Wessel [c]

[a] Dept. of Chemistry & Chemical Biology, and Brockhouse Institute for Materials Research, McMaster University, Hamilton, ON L8S 4M1, Canada
[b] Electron Microscopy Facility, McMaster Health Sciences, McMaster University, Hamilton, ON L8N 3Z5, Canada
[c] Ballard Power Systems Inc, 9000 Glenlyon Parkway, Burnaby, BC V5J 5J9, Canada

HIGHLIGHTS

- STXM is used to analyze polymer membrane fuel cell cathodes.
- Carbon corrosion and Pt-in-membrane degradation is tracked.
- Low surface area and medium surface area carbon supports are compared.
- Ionomer, Pt and carbon support are quantitatively mapped.
- F 1s and S 2p results show ionomer still present despite extensive C-corrosion.

GRAPHICAL ABSTRACT

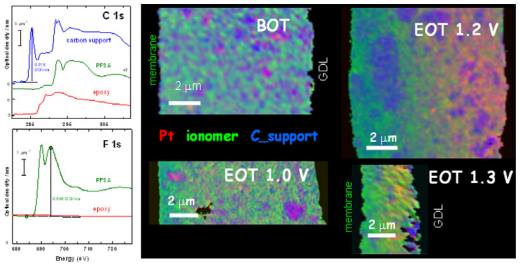

ARTICLE INFO

Article history:
Received 6 March 2014
Received in revised form
23 April 2014
Accepted 23 April 2014
Available online 14 May 2014

Keywords:
Polymer electrolyte membrane fuel cells
X-ray microscopy
Ionomer
Carbon corrosion
Platinum degradation

ABSTRACT

Scanning Transmission X-ray Microscopy (STXM) at the C 1s, F 1s and S 2p edges has been used to investigate degradation of proton exchange membrane fuel cell (PEM-FC) membrane electrode assemblies (MEA) subjected to accelerated testing protocols. Quantitative chemical maps of the catalyst, carbon support and ionomer in the cathode layer are reported for beginning-of-test (BOT), and end-of-test (EOT) samples for two types of carbon support, low surface area carbon (LSAC) and medium surface area carbon (MSAC), that were exposed to accelerated stress testing with upper potentials (UPL) of 1.0, 1.2, and 1.3 V. The results are compared in order to characterize catalyst layer degradation in terms of the amounts and spatial distributions of these species. Pt agglomeration, Pt migration and corrosion of the carbon support are all visualized, and contribute to differing degrees in these samples. It is found that there is formation of a distinct Pt-in-membrane (PTIM) band for all EOT samples. The cathode thickness shrinks due to loss of the carbon support for all MSAC samples that were exposed to the different upper potentials, but only for the most aggressive testing protocol for the LSAC support. The amount of ionomer per unit volume significantly increases indicating it is being concentrated in the cathode as the carbon corrosion takes place. S 2p spectra and mapping of the cathode catalyst layer indicates there are still sulfonate groups present, even in the most damaged material.

1. Introduction

Fuel cell durability has been identified as a key barrier to proton exchange membrane fuel cell (PEM-FC) commercialization. A major

* Corresponding author. Tel.: +1 905 525 9140x24749.
E-mail address: aph@mcmaster.ca (A.P. Hitchcock).

http://dx.doi.org/10.1016/j.jpowsour.2014.04.119
0378-7753/

factor contributing to the performance loss is the stability of the Pt catalyst and catalyst support. These factors are greatly influenced by operational conditions and the structure and composition of the catalyst layer and thus they are a major issue affecting the lifetime of the fuel cell, especially in automotive applications [1–6]. One of the operational conditions that is recognized as a major cause for voltage degradation is the shut-down/start-up condition of the fuel cell stack, where a H_2/air front in the anode can result in localized high cathode potentials. The catalyst, typically Pt or a Pt-alloy, is in the form of highly dispersed nanoparticles (2–4 nm) distributed over a carbon support, which consists of a dense but pore-filled network of particles (20–50 nm) that forms a conductive and porous structure. Platinum catalysts on different carbon support materials have been evaluated to identify those optimal for PEM-FC use. In this work, PEM-FC membrane electrode assemblies (MEAs) were prepared using two different types of Pt catalyst carbon support materials – a low surface area carbon (LSAC) and a medium surface area carbon (MSAC). The objective of this study was to understand the effect of high voltage excursions, which are typically encountered during start up/shut down operation, on cathode catalyst layer degradation mechanisms for Pt catalysts supported on LSAC and MSAC supports. We have applied soft X-ray scanning transmission X-ray microscopy (STXM) [7–9] to ultramicrotomed thin sections of MEAs in order to measure quantitative chemical maps of the constituent components, in particular the Pt catalyst, the ionomer and the carbon support in the cathode layer, using methods developed and described elsewhere [10–13]. STXM was applied to beginning-of-test (BOT) samples and to various types of end-of-test (EOT) samples that were subjected to different accelerated testing protocols.

Scanning transmission soft X-ray microscopy (STXM) [7–9] is a synchrotron based analytical microscopy that uses the natural X-ray absorption properties of the chemical species present to provide molecular speciation (i.e. bonding as well as elemental identification) and quantitative analysis at high spatial resolution (~30 nm routine, state-of-art is 10 nm [14]). For the past 5 years our group at McMaster University and others have been applying soft X-ray STXM methods to investigate a range of properties of PEM-FC materials [10–13,15–19]. Here we use STXM to investigate the changes in morphology, chemical composition and spatial distributions of components in PEM-FC MEAs caused by various testing protocols. A focus of the study was to probe the influence of the type of catalyst support (LSAC or MSAC) that was used in the two classes of PEM-FCs on catalyst layer compositional degradation. The major degradation phenomena in these tests was Pt agglomeration in the electrode, Pt migration into the membrane (PITM), and carbon corrosion, i.e. physical loss of carbon support material.

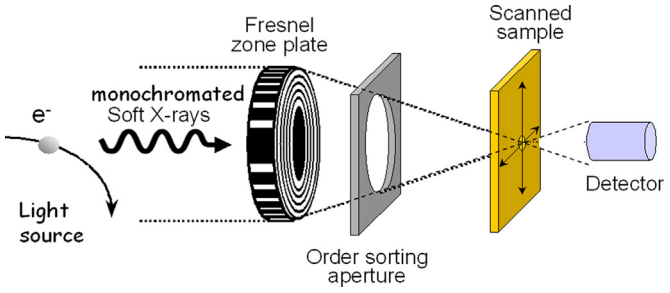

Fig. 1. Schematic of a scanning transmission X-ray microscope (STXM). X-rays produced by a storage ring (the bend magnet at ALS BL 5.3.2.2, or the elliptically polarizing undulator at CLS BL ID10.1) are monochromated by beamline optics and illuminate a Fresnel zone plate. A fraction (10–15%) of the X-rays are focused to a ~30 nm spot, where the sample is located. The zero-order (non diffracted) X-rays are blocked by the order sorting aperture. Images are acquired by detecting transmitted X-rays in single photon counting mode synchronously with raster scanning the sample.

This paper is organized as follows. The experimental section describes the samples and the accelerated testing procedures used, the method for STXM sample preparation, and the methods for STXM acquisition and data analysis. The results section starts by presenting the performance of the different catalysts under the accelerated stress testing. This is followed by detailed presentation of the STXM results, first those for the LSAC BOT, then LSAC EOT, followed by those for the MSAC BOT and MSAC EOT samples. Differences in results for the LSAC and MSAC series are discussed. Quantification of the ionomer in all 8 samples from the F 1s edge, and in two samples (LSAC BOT and LSAC EOT_1.3V) from the S 2p edge are reported. The discussion relates the STXM results to the performance and how the degradation differs with the two types of catalyst supports.

2. Experimental

2.1. Sample description and history

Membrane Electrode Assemblies (MEA) were made of a catalyst coated membrane (CCM) using a Pt loading of 0.4/0.1 mg cm^{-2} (cathode/anode), a commercial 50:50 wt.% Pt/C catalyst, and Nafion® ionomer. The CCM was manufactured in-house using the Nafion® NR211 membrane. The gas diffusion layers (GDL) were made by AvCarb using a continuous process. MEAs using two different catalysts were tested to compare the corrosion resistance of carbon supports; a graphitic low surface area carbon (LSAC) support of 180 $m^2\ g^{-1}$ surface area (BET) and a slightly less graphitic medium surface area carbon (MSAC) support of 250 $m^2\ g^{-1}$ surface area (BET). The test hardware used was designed to provide quasi-uniform operational conditions with the following features: bladder compression, high flow rates, liquid cooled temperature control, and carbon composite plates with parallel flow fields designed for low pressure and uniform flow, and an active area of 45 cm^2.

The cell was conditioned at standard steady state operating conditions prior to accelerated stress testing (AST) which accelerated the degradation of the cathode through voltage cycling under the following conditions: (cathode)/H_2 (anode) environment, voltage cycling from a lower potential limit of 0.6 V_{RHE} for 30 s, to various upper potential limits (UPL) of 1.0–1.4 V_{RHE} for 60 s. Performance diagnostics (polarization, cyclic voltammetry) was conducted after 0, 50, 700, 1400, 2100, and 4700 cycles. Scanning electron microscopy (SEM), X-ray Diffraction (XRD) and STXM analyses were performed on beginning-of-test (BOT) and degraded end-of-test (EOT) MEAs.

2.2. Sample preparation for STXM

The membrane electrode assemblies (MEA) from the BOT and EOT PEM-FC samples were cut into small rectangular (1 mm × 3 mm) pieces and embedded in an epoxy [20]. The embedded samples were cut at room temperature using a Leica Ultracut UCT ultramicrotome (Leica Mikrosystem, Wien, Austria). The nominal (target) thickness of the sections was 100 nm in order to have a peak optical density between 0.5 and 1.5 at the C 1s edge. However, due to the rubbery character of the membrane, the membrane part of the sections was significantly thicker, probably because that part of the sample was cut only on every third or fourth pass of the sample over the diamond blade. Several ultramicrotomed sections were deposited on a 100-mesh formvar-coated Cu TEM grid (~30 nm thickness of formvar film) [21]. Only sections with a reasonably intact membrane were examined by STXM.

2.3. STXM measurements

STXM data was measured on beamline 10ID1 at the Canadian Light Source [22] (CLS, Saskatoon,SK, Canada) and at beamline 5.3.2.2 [23] at the Advanced Light Source (ALS, Lawrence Berkeley National Laboratory (LBNL), CA, USA). Both STXMs are custom instruments [24]. The CLS 10ID1 undulator beamline covers 130–2700 eV with tunable polarization (left circular polarized light was used for all CLS measurements reported here). ALS 5.3.2.2 is a bending magnet beamline covering 250–1000 eV. Both beamlines provide a resolving power ($E/\Delta E$) better than 1500. The energy scale was calibrated using sharp lines of CO_2 measured in the STXM tank.

The details of the STXM instrument and its operation are described elsewhere [7–9]. A sketch indicating the basic components of STXM is presented in Fig. 1. Monochromatic X-rays from the beamline illuminate a Fresnel zone plate lens which focuses the X-rays to a ~30 nm spot. An order sorting aperture (OSA) is used to pass the first order diffracted X-rays while blocking the zeroth order (un-diffracted) light. The sample is positioned at the focal point of the zone plate. Those X-rays that pass through the sample are detected in single photon counting mode using a detector consisting of a phosphor to convert soft X-rays to visible light and a high performance photomultiplier to detect the visible photons. The zone plates for both instruments, which were made by the Center for X-ray Optics (LBNL) had 25 nm outer zone width, 240 μm diameter and a 90 μm central stop. The OSA was 50 or 60 μm in diameter. Images were measured with a dwell time of 1 ms per pixel. Images at a single X-ray energy are measured by recording the transmitted X-ray intensity, $I(X, Y, E)$ at each pixel in a user-selected area of the sample which is raster scanned with a piezo scanning stage. The samples are measured dry, in an environment of 0.1–0.2 atm of He.

Two types of analytical measurements were used. In one, a sequence of images (stacks [25]) over a range of photon energies (e.g. for C 1s, 80 images from 280 to 320 eV) were acquired from a relatively small area (typically 10 μm × 10 μm). In the second, a small number of images (four or five) at carefully selected energies in the C 1s and F 1s edges were measured over larger areas (typically 50 μm × 30 μm). The latter, called stack maps, provide higher statistical sampling and are the data used to derive the main results presented in this paper.

2.4. STXM data analysis

All data was analyzed using aXis2000 [26]. The measured transmission signals were first converted to optical density (OD) using the incident flux signal recorded through a clean formvar region of the same grid, just before or after the stack or stack map was recorded. The stacks or stack maps were then aligned using cross-correlation procedures in aXis2000. Quantitative chemical maps were derived from full stacks by singular value decomposition (SVD) fitting [27] to reference spectra placed on optical density per nm thickness scales (see Fig. 2). Note that in the context of STXM analysis thickness refers to the length of pure material at standard density that the X-rays pass through to give a specific OD. The generation of these optical density reference spectra from spectra recorded on the pure materials is outline in the supplemental material (see Supplemental section 1). Conversion of reference spectra to an absolute intensity scale relies on the fact that the optical density per nm thickness of a compound depends solely on the composition and density at energies below and far above the NEXAFS region [28]. The carbon support maps were derived from C 1s 2-energy stack maps from the difference between OD images recorded at 285.2 eV (peak of the graphitic carbon signal) and 278 eV (pre C 1s), multiplied by 0.016 (which is the

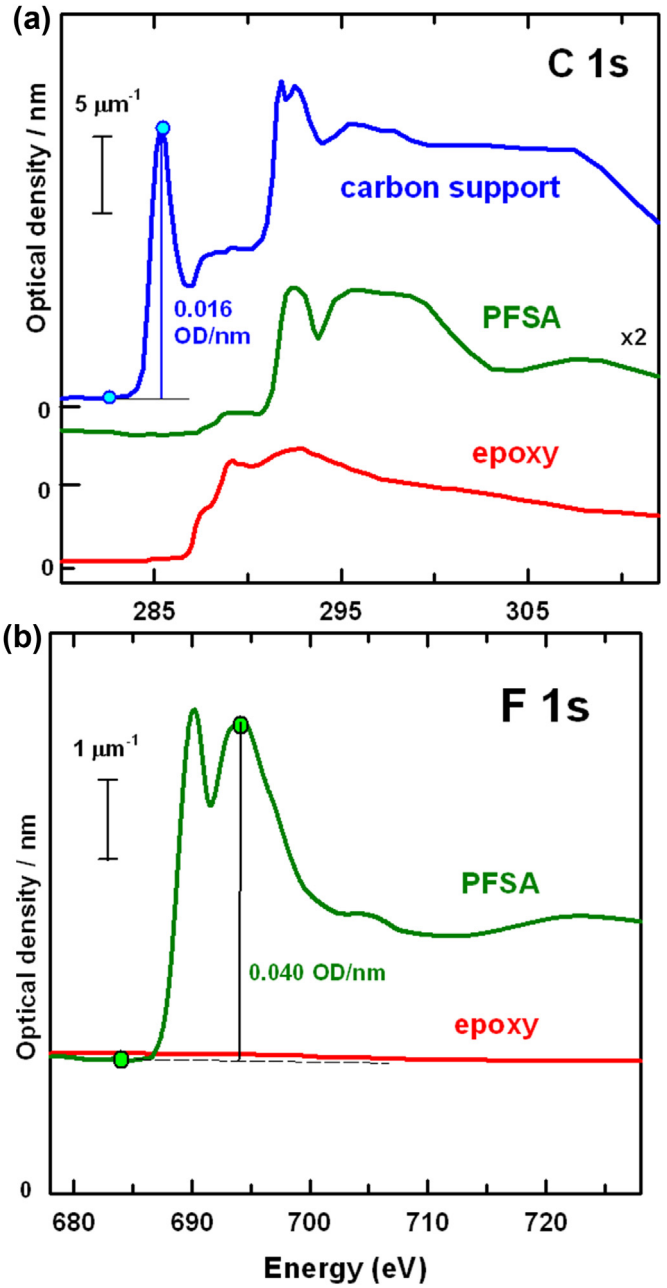

Fig. 2. (a) C 1s spectra of the carbon support, perfluorosulfonic acid membrane (PFSA) and the embedding epoxy, presented on an absolute intensity scale (optical density per nm (OD1) at standard density of the dry material). Note the PFSA spectrum has been expanded by a factor of 2 to better visualize its spectral features. The difference in OD/nm from the pre C 1s edge to the peak of the graphitic π* signal, ($OD_{285.2} - OD_{278}$), is 0.016. (b) F 1s spectra of the PFSA membrane and the embedding epoxy (that and the carbon support do not contain F), presented on an absolute OD1 intensity scale. The difference in OD/nm from the pre-F1s edge to the peak signal, ($OD_{694} - OD_{684}$), is 0.0040 [ALS 5322].

difference in the reference OD1 signal at these 2 energies, see Fig. 2) [10,12,15]. The fluorine maps, which contain the signals from both the membrane and the ionomer, were derived from F 1s 2-energy stack maps which are the difference between OD images recorded at 694 eV (peak of the perfluorosulfonic acid (PFSA) signal) and 684 eV (pre F1s), multiplied by 0.0040 (see Fig. 2). The catalyst amount (t_{Pt}) was derived from the 278 eV OD image, which is dominated by the signal from the heavy metal catalyst, which is pure Pt in these samples. There is a significant contribution at 278 eV OD signal from the F-rich ionomer. The ionomer

contribution is removed and the catalyst amount is derived using the formula

$$t_{Pt}(\text{nm}) = \frac{\text{OD}(278) - 0.425{*}F - \text{map}(\text{in OD})}{0.034} \quad (1)$$

where 0.425 is the ratio of the OD for the ionomer at 278 eV (0.0017), to that used to derived the F-map ($OD_{694} - OD_{684} = 0.0040$), and 0.034 is the OD at 278 eV of pure Pt at its bulk density. The sulfonate signal (from PFSA membrane and ionomer) was derived from fits of S 2p stacks to reference spectra placed on an OD1 intensity scale (OD/nm). Since the S 2p signal is quite weak and sitting on a large background, the quantitative accuracy is less for that edge.

In order to display the spatial correlations among the chemical components color coded composite maps were generated where the signal from each component was displayed in one of three primary colors – red – catalyst, green – ionomer, blue – carbon support. In all cases in this paper, the mapping from thickness scales to color scales was rescaled separately within each color. This approach gives best insight into spatial correlations of components. Where needed, the actual thickness scales for each component are also indicated by intensity color bars.

Other manipulations and quantitative measurements performed on the derived component maps include rotation (to present the data on a standardized view, with the cathode region oriented vertically with the membrane boundary on the left); masking – to isolate signals exclusively from the cathode region (cathode masks were typically derived from the carbon support maps by mask generation routines in aXis2000); generating histograms of the signal (which provides information about distributions of thickness of each component); calculating profiles of components across the vertically oriented cathodes by averaging the image pixels vertically over a range selected to be representative of the sample. As far as possible, standardized processing and presentation procedures were used.

3. Results and discussion

3.1. Catalyst type and performance

Fig. 3a shows TEM images of the two catalyst types investigated. The LSAC catalyst image reveals a high frequency of walls with a high graphitic content and large Pt agglomerates that are anchored along edges and at corners of the graphitic walls. In contrast,

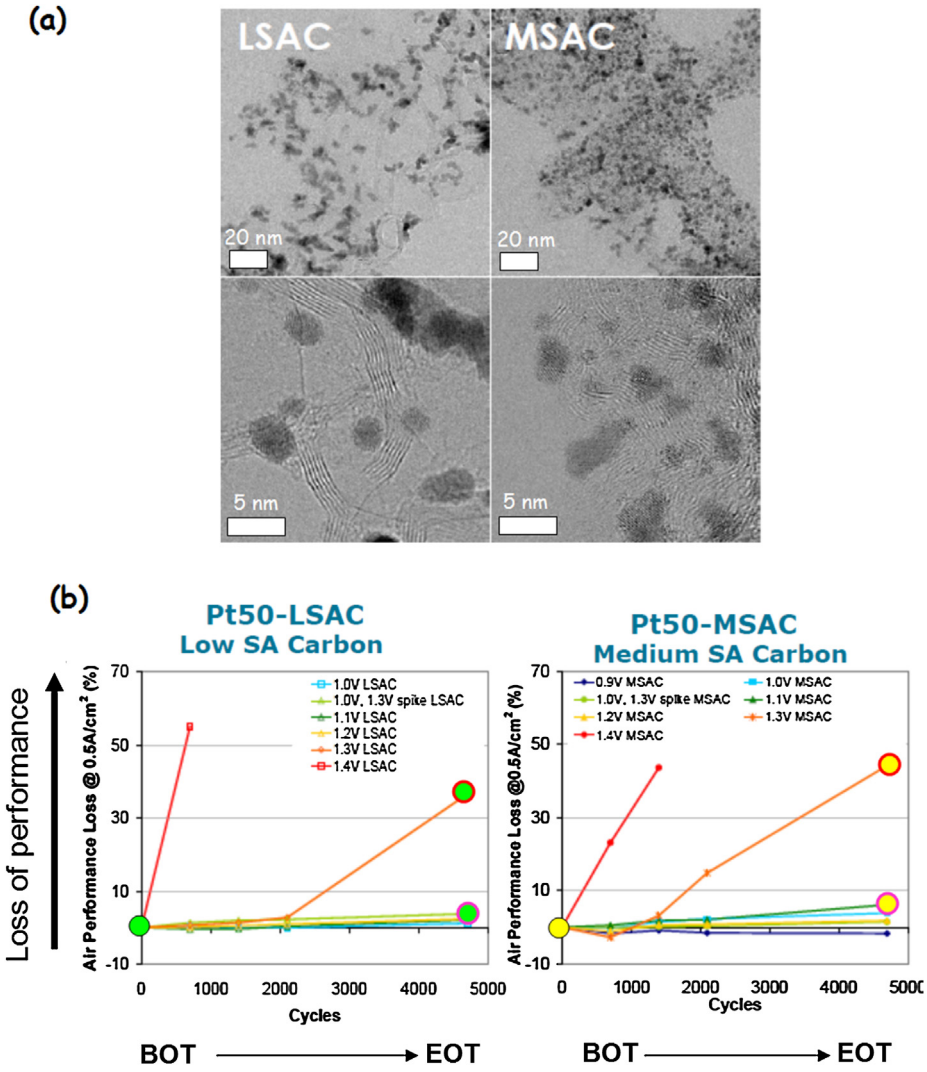

Fig. 3. (a) Transmission electron micrographs of the low surface area carbon (LSAC) and medium surface area carbon (MSAC) catalyst coated carbon support. These aberration corrected scanning transmission electron microscopy (STEM) images were acquired at the JEOL 2200FS microscope at the SHaRE user facility at Oakridge National Laboratory. (b) Performance plots of the LSAC and MSAC samples under specified cycling conditions [29]. The circles indicate the samples examined by STXM.

graphitic centers are observed throughout the carbon structure of the MSAC catalyst and the Pt particles are better dispersed. Furthermore, evaluations of agglomerate sizes and shapes from these images indicate that the LSAC catalysts have a narrower particle size distribution than the MSAC catalyst and that the LSAC Pt particles were somewhat elongated, while the MSAC Pt particles were mostly round in nature.

Fig. 3b shows the performance loss of the different MEAs after they were exposed to cathode voltage cycling at various upper potential limits (UPL) for 4700 cycles (designated as EOT = end-of-test). Both the LSAC and MSAC MEA showed similar BOT performance. They also revealed a similar voltage degradation signature as a function of UPL, i.e. the voltage degradation increases with increasing upper potential and prolonged cycling. For UPLs greater than 1.2 V, the primary degradation mechanism shifts from predominantly Pt dissolution to predominately carbon corrosion at which point the cathode catalyst layer thickness begins to shrink substantially [29]. A comparison of the two MEAs shows that the LSAC catalyst is more stable at the 1.3 V UPL, as the onset of corrosion is observed at a larger cycle number than that for the MSAC catalyst [29].

Fig. 4a–c summarizes the effect of UPL on the effective electrochemical surface area (ECSA), Pt particle growth (agglomeration) and change in catalyst layer thickness (support corrosion), respectively [29]. The loss in effective catalyst surface area (ECSA) with progressive accelerated stress test (AST) cycling at various UPLs, shown in Fig. 4a, reveals similar trends for the MSAC and LSAC Pt catalysts, with severe ECSA loss at the higher potentials which is likely associated with Pt detachment from the support. While the ECSA losses were essentially the same for both catalysts after cycling at 1.2 V UPL, at UPLs above and below 1.2 V the per cent ECSA loss as a function of cycle number deviates for the LSAC and MSAC catalysts. At an UPL $<$ 1.2 V, where the primary degradation mechanism is Pt dissolution, the MSAC based catalyst showed a lower ESCA loss compared to the LSAC based catalyst. The opposite trend (ECSA loss: MSAC $>$ LSAC) has been observed for the AST with UPL $>$ 1.2 V, at which point carbon corrosion becomes the dominate degradation mechanism. This indicates that the carbon structure has an impact on the degradation of Pt and carbon. The HRTEM observations (Fig. 3) described above indicate a better Pt particle dispersion on the MSAC compared to LSAC support, which would affect the rate of Pt dissolution and agglomeration at low UPLs.

Fig. 4b reveals that at UPL $<$ 1.2 V the EOT particle size for the MSAC catalyst is slightly smaller compared to the LSAC catalyst, which is consistent with the observed lower ECSA loss. At UPL $>$ 1.3 V, both catalysts show an insignificant change in Pt particle size and similar particle size growth with increasing UPL. Furthermore, Fig. 4c shows that the rate of cathode layer thinning and thus carbon corrosion increases as a function of UPL and that the carbon supports begin to degrade at potentials between 1.0 and 1.2 V. A comparison of the two catalysts indicates that the graphitized LSAC catalyst is more stable at an UPL of 1.3 V and less stable at UPL $\geq$ 1.4 V compared to the MSAC. It is believed that the graphitization level and structure of the different supports impact the rate of catalyst thinning at higher potential. As observed from HRTEM analysis (Fig. 3a) the walls and internal structure of the LSAC and MSAC supports are very different. The highly graphitized surface walls with an amorphous center characteristic of the LSAC support would suggest that corrosion takes place at the center of the carbon agglomerates, causing the walls to collapse after prolonged corrosion. In contrast, the MSAC structure exhibits agglomerates with fewer graphitic walls that are more broken; thus one would expect more uniform thinning of carbon agglomerates.

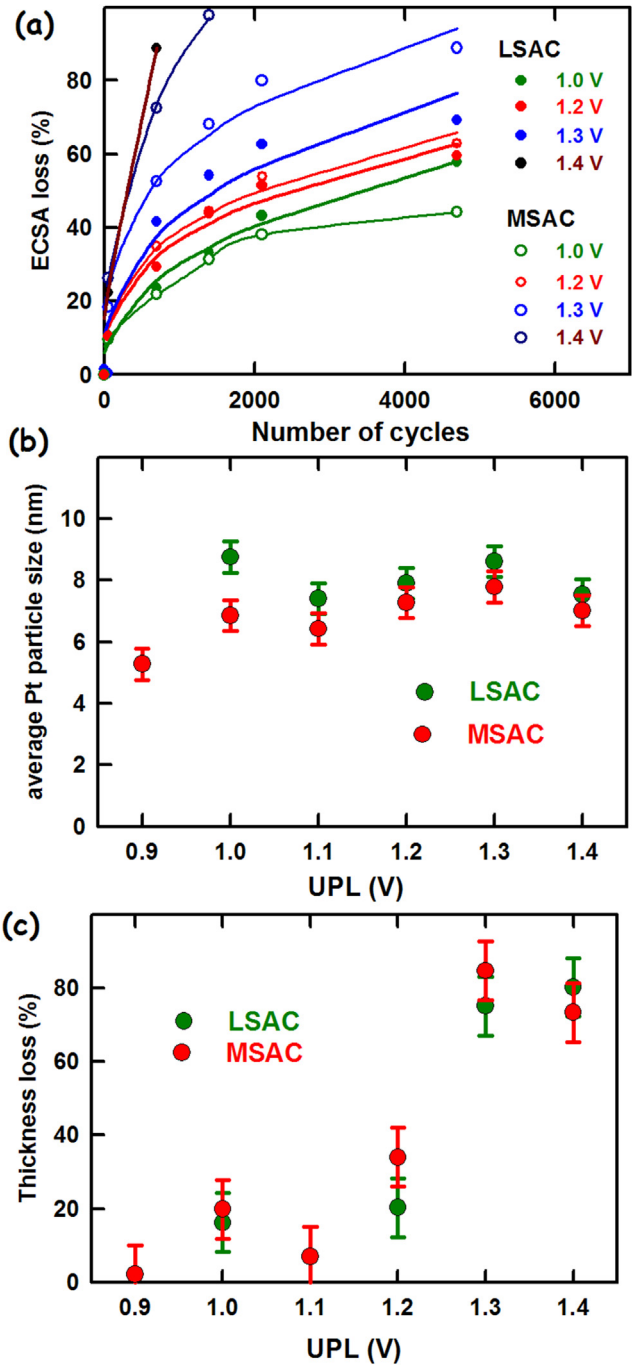

Fig. 4. (a) Effective electrochemical surface area (ECSA) as a function of the number of cycles, for the different upper potential levels (UPL) and catalyst supports. (b) Pt particle size as a function of UPL for the two catalyst supports. (c) Change in catalyst layer thickness due to carbon support corrosion, as a function of UPL, for the two types of catalyst supports.

3.2. LSAC BOT analysis

Fig. 5 is an example of the data and the analysis procedure used to derive quantitative component maps from STXM images recorded at four energies. Fig. 5a and b are STXM images of the LSAC BOT sample recorded at 278 and 285.2 eV after conversion to an optical density (OD) scale. The numbers at the upper and lower right of each image indicate the OD limits of the gray scale display. Since only the carbon support absorbs at 285.2 eV the difference of these

images, ($OD_{285.2}$ − OD_{278}) is quantitatively related to the carbon support. This difference signal is plotted as Fig. 5c, after masking it so as to display only the cathode and anode regions. The electrode-only mask used to isolate the signal from only the electrodes is readily generated by using the histogram thresholding tool in aXis2000. The mean thickness of the carbon support in the cathode is 36 ± 6 nm, while that in the anode is 18 ± 5 nm, based on a conversion of 0.016OD/nm (see Fig. 2). Fig. 5d and e presents STXM OD images at 684 and 694 eV for the LSAC BOT sample, while Fig. 5f presents the difference (OD_{694} − OD_{684}) masked to the electrodes only. The OD_{694} − OD_{684} signal is a quantitative map of the ionomer in the electrodes, based on a conversion of 0.0040OD/nm (see Fig. 2). Aside from a few bright spots from agglomerated carbon particles, the carbon support map is relatively uniform. In contrast the ionomer is much less uniform, with some ovoid regions which are significantly depleted in ionomer. Detailed spectral analysis of these regions based on full C 1s stacks confirms that the depletion in the ovoid regions is specifically in the ionomer component (see

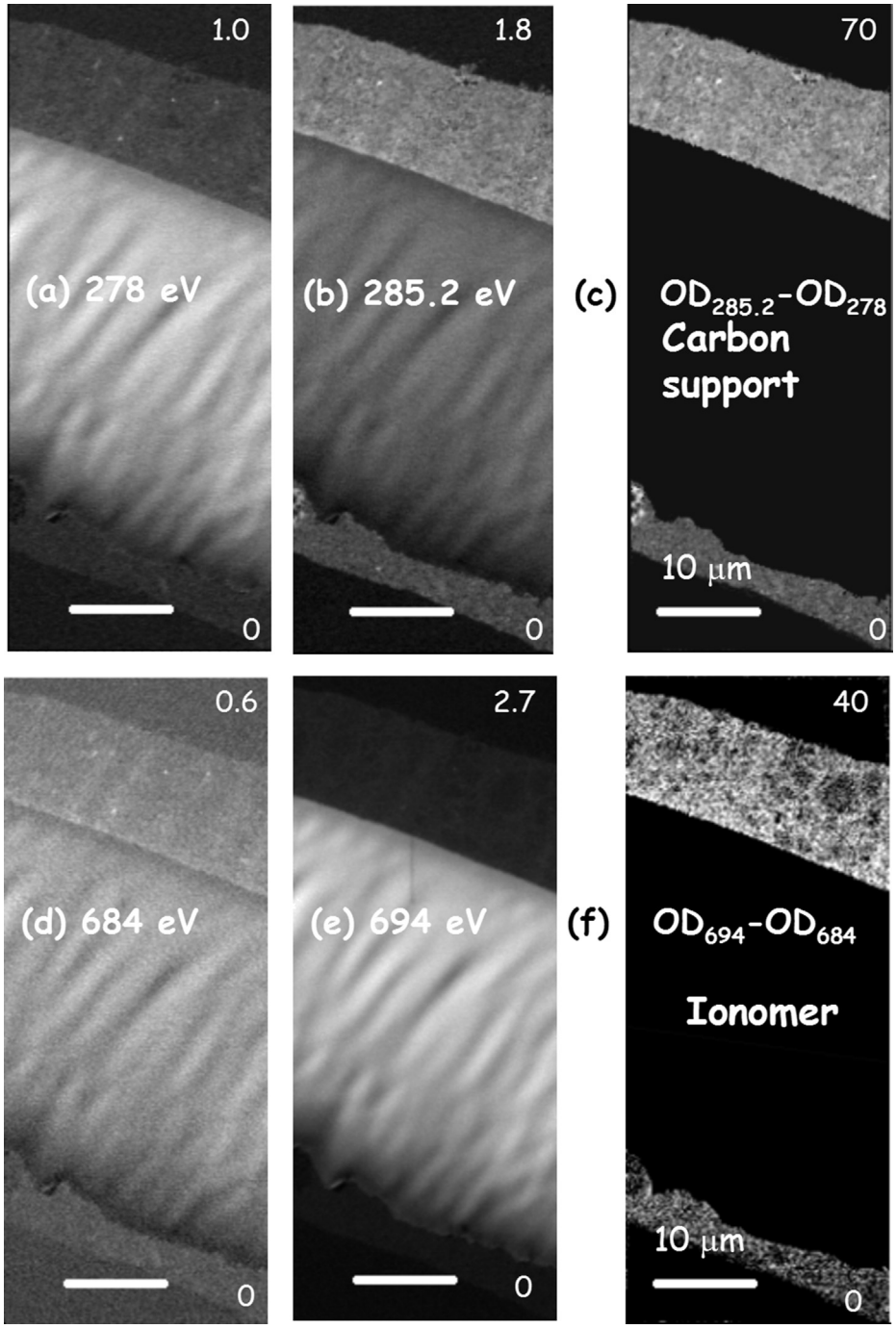

Fig. 5. Optical density (OD) STXM images at (a) 278 eV and (b) 285.2 eV for the LSAC BOT sample, and, (c) the difference ($OD_{285.2}$ − OD_{278}), masked to the electrodes only. The gray scale of the difference image is thickness in nm of the carbon support material, based on a conversion of 0.016OD/nm. STXM OD images at (d) 684 eV and (e) 694 eV for the LSAC BOT sample, and, (f) the difference (OD_{694} − OD_{684}) masked to the electrodes only. The gray scale of this difference image is thickness in nm of the ionomer, based on a conversion of 0.0040 OD/nm (see Fig. 3) [ALS 5322].

Supplemental section 2). These ovoid features are most likely a result of mixing or coating issues with the catalyst ink.

Fig. 6 (left column) presents quantitative maps of the carbon support, catalyst (pure Pt) and ionomer in the cathode of the LSAC BOT, derived from the carbon and fluorine maps which were in turn, derived from STXM OD images at 4 energies (see Fig. 5). The gas diffusion layer (GDL) and the membrane (location identified by labels) have been excluded from these maps by applying a cathode-specific mask. The numbers at the upper and lower right of each map indicate the thickness range in nm of the gray scale display.

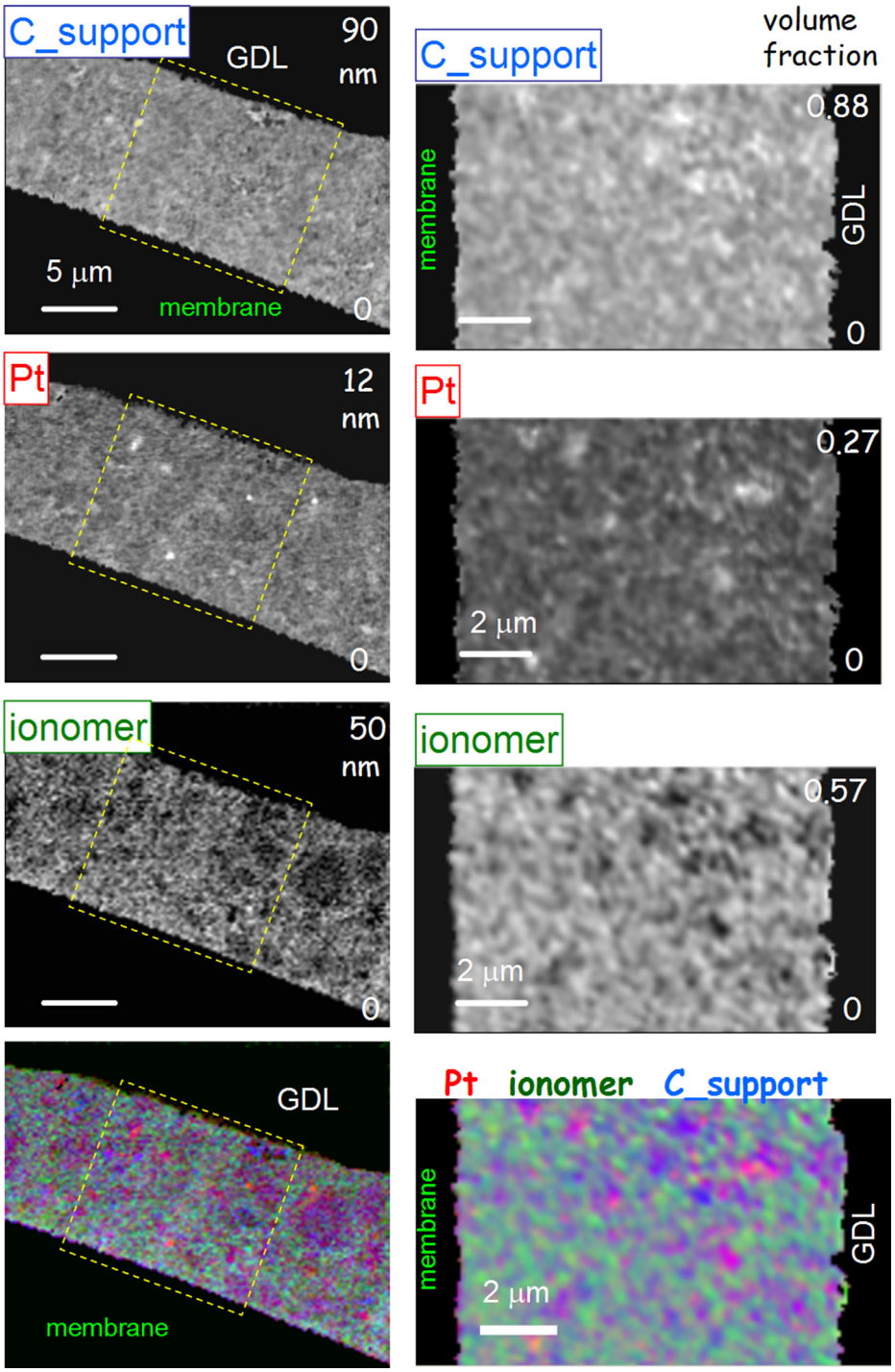

Fig. 6. (left column) Maps of the carbon support, catalyst (pure Pt) and ionomer in the cathode of the LSAC BOT, derived from STXM OD images at 4 energies (see Fig. 2). The supporting medium and the membrane (locations identified by labels) have been excluded from these maps by applying a cathode-specific mask. The numbers at the upper and lower right of each map indicate the thickness range in nm. The lower left image is a color composite of the 3 component maps (rescaled so the signal for each species fills the full 0–255 color range) (red – catalyst, green–ionomer, blue – carbon support). (right column) Volume fraction images of the area, indicated by dashed yellow rectangles in the left column figures, for the components and the color composite. The volume fraction is the ratio of each component map to the sum of the three component maps. The images have been rotated to present them in a vertical orientation with the membrane side of the cathode to the left. This standard presentation is used in all other figures in this paper [ALS 5322]. (For interpretation of the references to color in this figure legend, the reader is referred to the web version of this article.)

The lower left image is a color composite of the 3 component maps (rescaled so that the signal for each species fills the full 0–255 range for each color) using red for the catalyst, green for the ionomer and blue for the carbon support.

In order to reduce the influence of different sample thicknesses throughout the 8 samples presented in this work, the individual component maps have been converted to volume fraction images by dividing each component map by the sum of the three component maps. The sum of thicknesses (volumes) of the three component maps is less then the actual volume of the electrode to the extent of the physical pore volume, which is mostly filled with epoxy in these sections. We chose this approach to generate volume fractions since it allow comparisons of microtome cuts with different thicknesses. The stack map analysis is very accurate because it measures signals specific to the 3 components (catalyst, support and ionomer) which are present in the original sample, and has little sensitivity to the embedding epoxy (see Supplemental section 3). These "reduced" volume fractions could be compared to the loading values for the materials, taking into account their gravimetric densities. The volume fraction images in the area indicated by the dashed yellow rectangle for the component and color composite maps in the left column are presented in the right column of Fig. 5. The volume fraction images have been rotated to present them in a vertical orientation with the membrane side of the cathode to the left. This standard presentation is used in all other figures of this type in this paper. The region chosen avoids most of the ionomer depleted ovoid regions since we believe these features are not representative of the majority properties of the sample. Catalyst and carbon support agglomerations are clearly visible in the map; sometimes but not always, they are spatially correlated, as indicated by a purple color in the color coded composite.

Fig. 7a presents histograms of the thickness, in nm, of the catalyst, ionomer and carbon support signals, and their sum, in the LSAC BOT cathode. These histograms were derived from the cathode area inside the yellow dashed rectangle in the component maps displayed in the left column of Fig 6. The breadth of the profiles reflects the distribution of thicknesses of the total and individual components, and is not a reflection of statistical uncertainties in the measurement. Despite using a mechanical cutting procedure (ultramicrotomy with a diamond knife) the width of the total thickness is broader than that of any individual component. This probably reflects the distribution of the porosity (which, in these samples, is mostly filled with the embedding resin, and thus complements the material of the original MEA – see Supplemental material, section S-3). Fig. 7b presents volume fraction profiles of the catalyst, ionomer and carbon support signals across the cathode (the origin of the horizontal axis is the membrane-cathode boundary) in the LSAC BOT cathode obtained by integrating horizontal line profiles over the full height of the volume fraction images in the right column of Fig. 6. This analysis indicates a very uniform distribution of all three components across the whole LSAC BOT cathode.

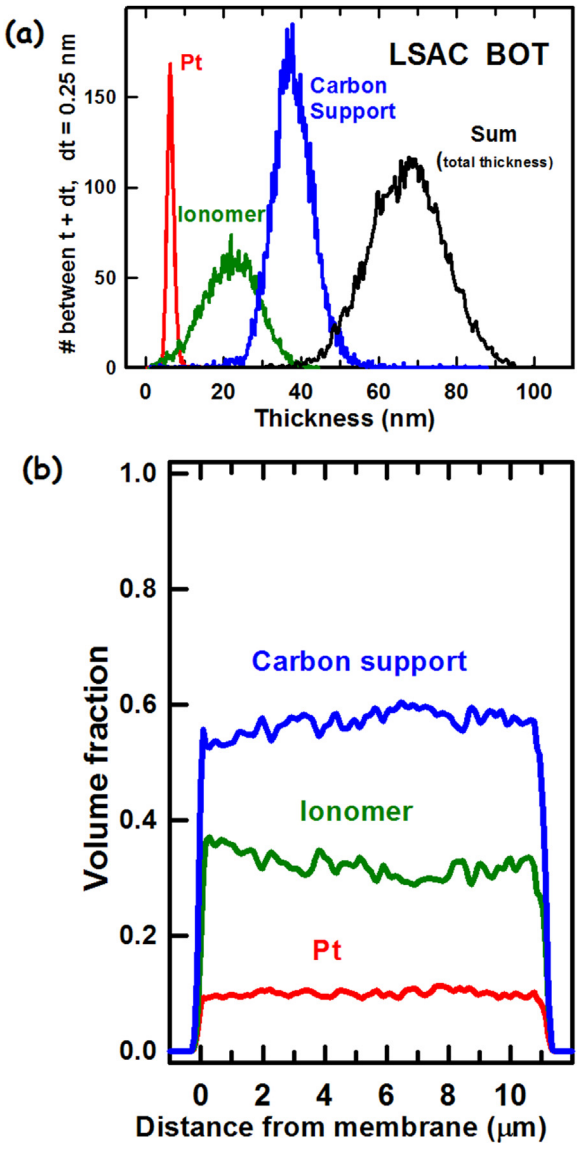

Fig. 7. (a) Histograms of the catalyst, ionomer and carbon support thicknesses (in nm) in the LSAC BOT cathode (see Fig. 6, right panel), and their sum. The breadth of the histogram signals reflects the distribution of thicknesses. (b) Profiles (nm) of the catalyst, ionomer and carbon support signals in the LSAC BOT cathode integrated over the full vertical height of the images in the right panel of Fig. 6 [ALS 5322].

3.3. LSAC – analysis of EOT at 1.0 V, 1.2 V and 1.3 V

Fig. 8 presents color composite images of the component maps for the Pt (red), ionomer (green) and carbon support (blue) in the cathode for the LSAC BOT and the three EOT samples which had undergone accelerated stress testing at upper potentials of 1.0, 1.2 and 1.3 V. The component maps were derived from the C 1s and F 1s 4-energy stack map approach outlined for the LSA_BOT sample in the preceding section. In order to compensate for any differences in section thicknesses, the component maps were converted to volume-fractions by dividing each component map by the sum of the three component maps. Each color scale is rescaled to use the full color range; the volume fraction limits for each component are indicated in Fig. 8. The data has been rotated so that the membrane – cathode boundary is vertical and to the left. The same spatial scale is used for each of the four color composite maps.

Comparison of these four maps reveals that key chemical changes are taking place in the carbon corrosion testing protocol (UPL = 1.3 V). The carbon corrosion effect is clear from the significantly reduced thickness of the cathode after the 1.3 V testing protocol. There is little reduction in cathode thickness for the other two testing protocols. There is a consistent increase in the volume fraction of ionomer through the BOT – 1.0, 1.2, 1.3 EOT series, indicating that the ionomer is mostly retained, even though the carbon support is being oxidized and lost. We note that thus this observation is specific to the backbone and side chains of the ionomer since it was determined from the F 1s signal. The S 2p measurements (see Section 3.6) address the issue of possible changes in

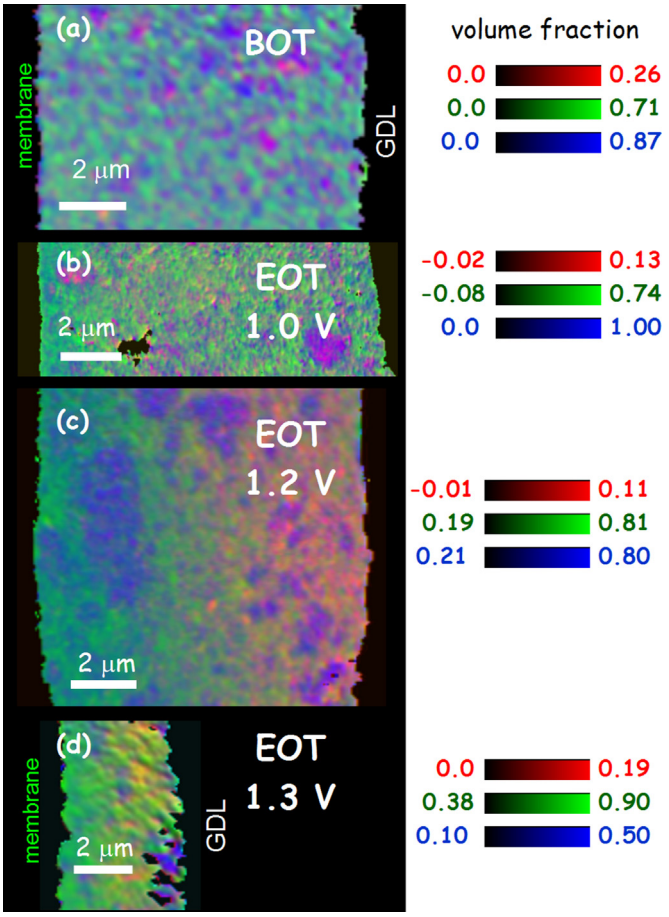

Fig. 8. Color composite images (red – catalyst, green – ionomer, blue – carbon support) of the volume fractions of the catalyst (pure Pt), carbon support and ionomer components in the cathode for the LSAC BOT and LSAC EOT 1.0, 1.2, 1.3 V samples, derived from the C 1s and F 1s 4-energy approach. The component maps were converted to volume fraction to correct for differences in the sample thickness. The color coded scale bars to the right give the range in volume fraction of each component. The measured data have been rotated so that the membrane – cathode boundary is vertical and to the left. The same spatial scale is used for each of the four composites [ALS 5322 & CLS]. (For interpretation of the references to color in this figure legend, the reader is referred to the web version of this article.)

the sulfonate amounts. The EOT 1.2 V composite map shows the Pt depletion layer clearly. It is also visible in the EOT 1.3 V composite map (the composite map is less red/more green on the side by the membrane), but it is harder to see as the Pt has been compressed into a smaller area. There is very little evidence of Pt depletion at the membrane catalyst layer interface in the EOT 1.0 V sample even though a PTIM band was seen in the membrane (see Supplemental material, section 4). In general, PTIM degradation is smaller for the 1.0 V UPL samples, and the trends in PTIM degradation with UPL are similar for the LSAC and MSAC samples. The maps presented in Fig. 8 clearly indicate that Pt dissolution is the dominant degradation mechanism for 1.0 and 1.2 V UPL while carbon corrosion become a major factor for UPL > 1.2 V. The images in Fig. 8b and c show that the Pt depletion layer is closer to the membrane while the carbon support is still stable and able to maintain the initial integrity for the electrode. For the 1.2 V and 1.3 V UPL range the major degradation is carbon dissolution, as indicated by images Fig. 8d versus c.

Fig. 9a–c presents profiles across the cathode (from the membrane side to the GDL side) of the volume fraction of the carbon support, Pt and ionomer signals respectively of the LSAC BOT and

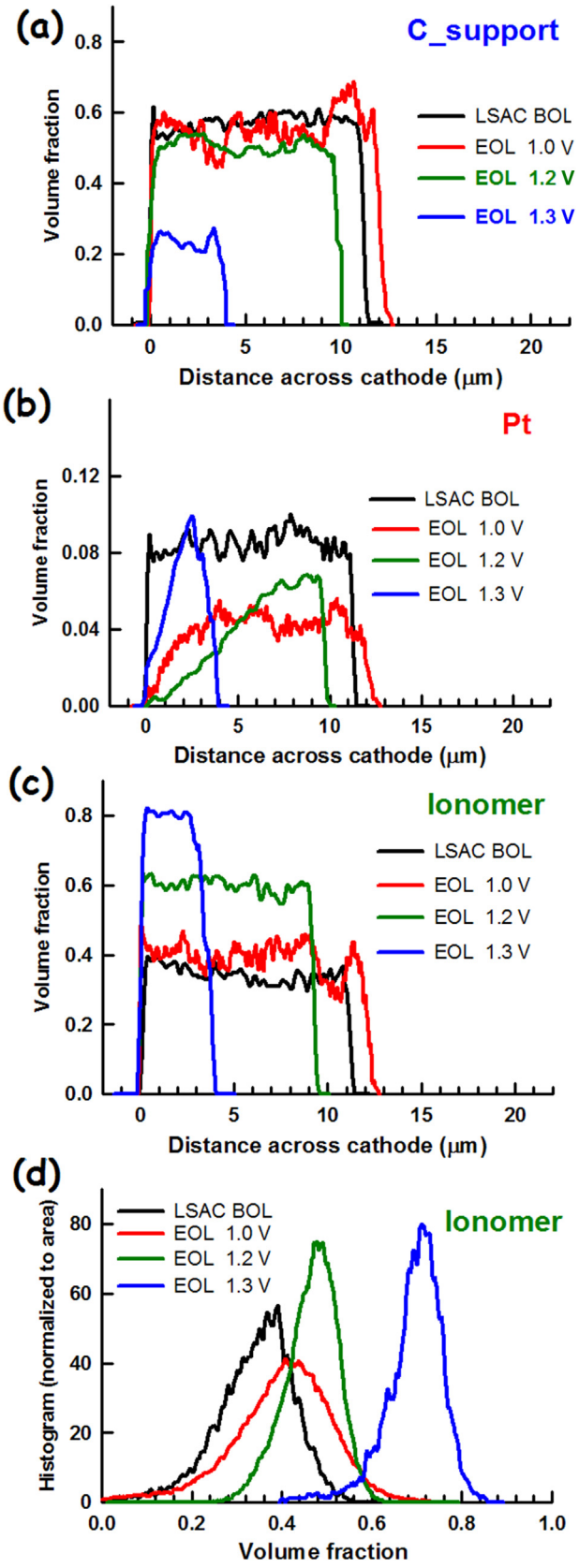

Fig. 9. Profiles of the volume fraction of (a) the carbon support, (b) Pt catalyst and (c) ionomer signals across the cathode of the LSAC BOT and LSAC EOT 1.0, 1.2, 1.3 V samples integrated vertically over the areas displayed in Fig. 7. (d) Histograms (normalized to number of pixels) of the ionomer volume fraction for the LSAC BOT and EOT 1.0, 1.2, 1.3 V samples [ALS 5322 & CLS].

1.0, 1.2, 1.3 V EOT samples, integrated vertically over the areas displayed in Figs. 6 and 8. The origin of the distance scale is the membrane-cathode boundary. The reduction of the width of the cathode due to carbon corrosion is clearly seen in the reduced width of the EOT 1.2 V and especially, the EOT 1.3 V profile. Fig. 9d shows the histograms of the volume fraction for ionomer in the cathode for all 4 samples. The centroids of the histograms are 0.37, 0.42, 0.48 and 0.72 for the LSAC BOT and 1.0, 1.2, 1.3 V EOT samples respectively. This clearly shows that the ionomer is being redistributed through the electrode and concentrated due to the decrease in the electrode thickness caused by the carbon corrosion process.

In order to determine if ionomer was lost during stress testing, we examined the product of the mean volume fraction and the cathode width (see Table 1). By this measure the amount of ionomer per area is similar in the BOT, EOT 1.0 and EOT 1.2 V samples, but decreases by about a factor of 2 in the EOT 1.3 V sample. Of course this is based on the F 1s measurement which is sensitive to the ionomer backbone and side chains but not to the critical sulfonic acid groups. In order to check if the ionomer lost sulfonic groups in the stress testing we also examined the S 2p edge – see Section 3.6 below.

3.4. MSAC versus LSAC – C 1s spectra

Fig. 10 presents the C 1s spectra of the pure LSAC and MSAC supports on an absolute intensity scale (optical density per nm (OD1), acquired from the carbon support particles without the Pt catalyst. TEM images (see Fig. 3a) indicate that the graphitic character of the LSAC support is somewhat larger than that of the MSAC support. Surface analysis by X-ray photoelectron spectroscopy (XPS) of the conditioned catalyst layers also indicates a larger graphitic carbon fraction at the surface for LSAC, i.e. of 43% vs. 38% for MSAC. However the C 1s spectra measured by STXM indicate that the 285 eV π^* peak area for the MSAC sample is ~4% larger than that for LSAC, suggesting the reverse relationship in terms of graphitic content. However the differences in LSAC and MSAC signals in both XPS and STXM are very small, and may not be statistically significant.

3.5. MSAC – analysis of BOT and EOT at 1.0 V, 1.2 V and 1.3 V

Fig. 11 presents color composite images of the Pt, ionomer and carbon support in the cathode for the MSAC BOT and 1.0, 1.2, 1.3 V EOT samples. The measured data have been rotated so that the membrane – cathode boundary is vertical and to the left. The same spatial scale is used for each of the four composites. It can be seen that the width of the cathode is decreasing with increasing EOT voltage, at a more rapid rate than with the LSAC samples (compare Figs. 8 and 11). The 1.3 V EOT MSAC sample shows a drastic decrease in the cathode thickness to ~4 microns (Fig. 11d) from ~20 microns cathode width in the BOT (Fig. 11a). Another consequence of the higher cycling voltage is the presence of a platinum depletion layer next to the membrane/cathode interface and the generation of a PTIM band. It can be seen from the color composites that there is a lack of the red component in the area adjacent to the membrane in the 1.2 and 1.3 V EOT MSAC samples. A PTIM band was detected in the membrane for these samples (see Supplemental section 4).

Table 1
Cathode thickness (μm), mean volume fraction of the ionomer and their product.

Sample	W <thickness> (μm)[a]	V <vol. fraction>[b]	$W * V$
LSAC BOT	11.2	0.37	4.1
LSAC EOT 1.0 V	12.0	0.42	5.0
LSAC EOT 1.3 V	9.7	0.48	4.7
LSAC EOT 1.3 V	3.8	0.72	2.7
MSAC BOT	20.0[c]	0.25	5.0
MSAC EOT 1.0 V	16.0[c]	0.30	4.8
MSAC EOT 1.3 V	11.9	0.38	4.5
MSAC EOT 1.3 V	3.7	0.74	2.7

[a] from profile of the carbon support – see Fig. 9a for LSAC; 12a for MSAC.
[b] from histograms of the volume fraction of the ionomer – see Fig. 9d for LSAC; 12d for MSAC.
[c] These values are those measured for the STXM microtomed sections. Independent, non-STXM measurements on other samples indicate a cathode thickness of only 14 μm for MSAC BOT. This could indicate the pieces of MSAC MEA for the BOT and EOT 1.0 V were tilted when put into the epoxy and microtomed.

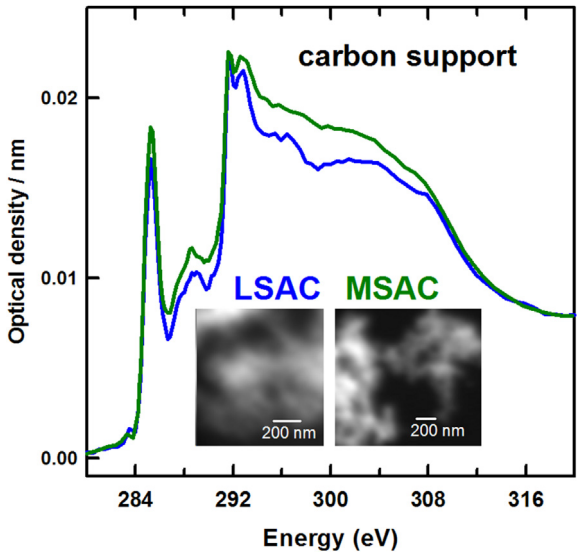

Fig. 10. C 1s spectra of pure LSAC and MSAC carbon support particles (without added catalyst) presented on an absolute intensity scale (optical density per nm (OD1) assuming a density of 2.0. The insets are STXM OD images at 285.2 eV of the areas from which these spectra were acquired. Individual carbon particles are visible in the MSAC but not in the LSAC sample [CLS].

Fig. 12a–c presents profiles of the volume fraction of the catalyst, ionomer and carbon support signals across the cathode of the MSAC BOT and 1.0, 1.2, 1.3 V EOT samples integrated over the areas displayed in Fig. 10. The drastic decrease in the catalyst layer thickness of the 1.3 V EOT can be correlated with the decrease of the carbon support volume fraction in Fig. 12a. The remaining ionomer is then concentrated in the reduced cathode width which leads to a large increase in the ionomer volume fraction in the 1.3 V EOT sample as can be seen in Fig. 12c. Fig. 12b shows that there is a platinum depletion layer in the 1.2 and 1.3 V EOT samples. The cathode layer adjacent to the membrane shows the least amount of Pt and the Pt level increases away from the cathode/membrane interface. These results are very similar to the ones found in the LSAC EOT samples. Fig. 12d plots the histograms of the volume fraction for ionomer in the cathode for all 4 MSAC samples. The area of each histogram has been normalized to the total signal of each type. The centroids of the histograms are 0.25, 0.30, 0.38 and 0.74 for the MSAC BOT and 1.0, 1.2, 1.3 V EOT samples respectively, indicating the volume fraction (concentration) of the ionomer is increasing as the cathode decreases in width due to carbon corrosion, similar to the changes observed in the LSAC samples.

3.6. Mapping of sulfonate groups in the LSAC – BOT and LS A1.3 V EOT

Fig. 13a presents a color coded composite of the Pt, ionomer and carbon support component maps for the LSAC BOT cathode, derived

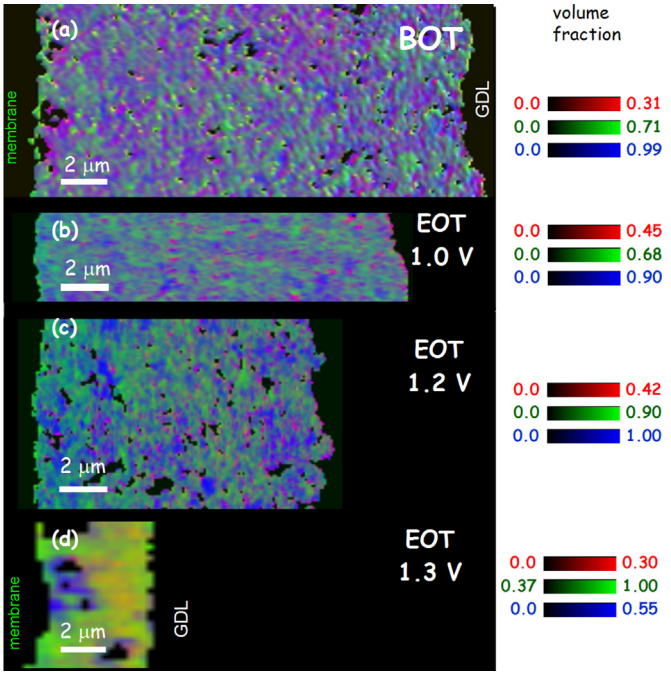

Fig. 11. Color composite images (red – catalyst, green – ionomer, blue – carbon support) of the carbon support, catalyst (pure Pt) and ionomer components in the cathode for the MSAC BOT and MSAC EOT 1.0, 1.2, 1.3 V samples. The component maps were converted to volume fraction to correct for differing sample thickness. The color coded scale bars to the right give the volume fraction range of each component. The measured data have been rotated so that the membrane – cathode boundary is vertical and to the left. The same spatial scale is used for each of the four composites [CLS & ALS 5322]. (For interpretation of the references to color in this figure legend, the reader is referred to the web version of this article.)

from the C 1s and F 1s 4-energy image approach. The BOT measurement provides a same-location reference for the S 2p based sulfonate analysis. Fig. 13b presents horizontal profiles of the thickness (nm) of the catalyst, ionomer and carbon support signals across the cathode. The amounts and horizontal profiles are in good agreement with the data presented earlier in this paper. Fig. 13c presents the S 2p NEXAFS spectra of the membrane of LSAC BOT and the spectra in the S 2p region of the epoxy and the carbon support, neither of which contain S. The OD1 intensity scale was derived by matching the intensities from 155 to 165 and above 196 eV to the OD1 signal for the elemental composition for Nafion-211 [28,30]. Fig. 13d is the map of the sulfonate signal in the cathode and membrane region of the LSAC BOT derived from a S 2p image sequence, fit to the reference spectra in Fig. 13c. Given the larger quantization uncertainties for the S 2p edge, the PFSA OD thickness in the membrane derived from this analysis is in reasonable agreement with that determined from the F 1s map, but the amount of ionomer in the cathode determined from S 2p data was 3–4 times larger than that determined from the F 1s analysis.

Fig. 13e is the color coded composite of the Pt, ionomer and carbon support component maps for the cathode for the LSAC EOT 1.3 V, derived from the C 1s and F 1s 4-energy image approach. Fig. 13f is the map of the sulfonate signal in the cathode and adjacent membrane of the LSAC EOT 1.3 V, derived from the S 2p image sequence, using the reference spectra in Fig. 13c. The PFSA levels in the membrane determined from the S 2p analysis are quite similar to those determined from the F 1s analysis. Fig. 13g is the horizontal profiles of the thickness (nm) of the PFSA/ionomer across the cathode and membrane extracted from the sulfonate maps in Fig. 13c and f. The sulfonate amount is about twice as large in the LSAC EOT 1.3 V sample as in the LSAC BOT sample, which is a trend consistent with concentration of the ionomer into a smaller electrode volume as carbon corrosion proceeds. The increase in the ionomer thickness estimated from the sulfonate signal (Fig. 13g) is ~2, less than the factor of ~3 reduction in the cathode thickness,

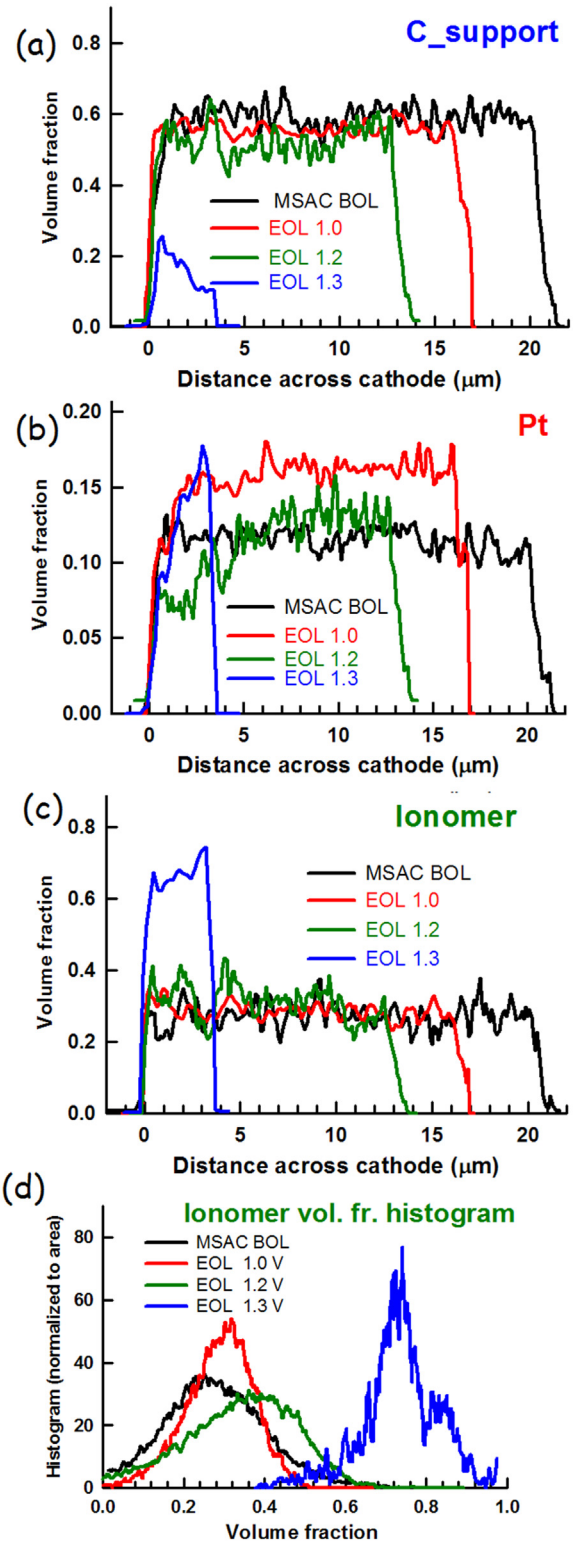

Fig. 12. Profiles of the volume fraction of (a) the carbon support, (b) Pt catalyst and (c) ionomer signals across the cathode of the MSAC BOT and MSAC EOT 1.0, 1.2, 1.3 V samples, integrated vertically over the areas displayed in Fig. 10. (d) Histograms (normalized to number of pixels) of the ionomer volume fraction for the MSAC BOT and MSAC EOT 1.0, 1.2, 1.3 V samples [CLS & ALS 5322].

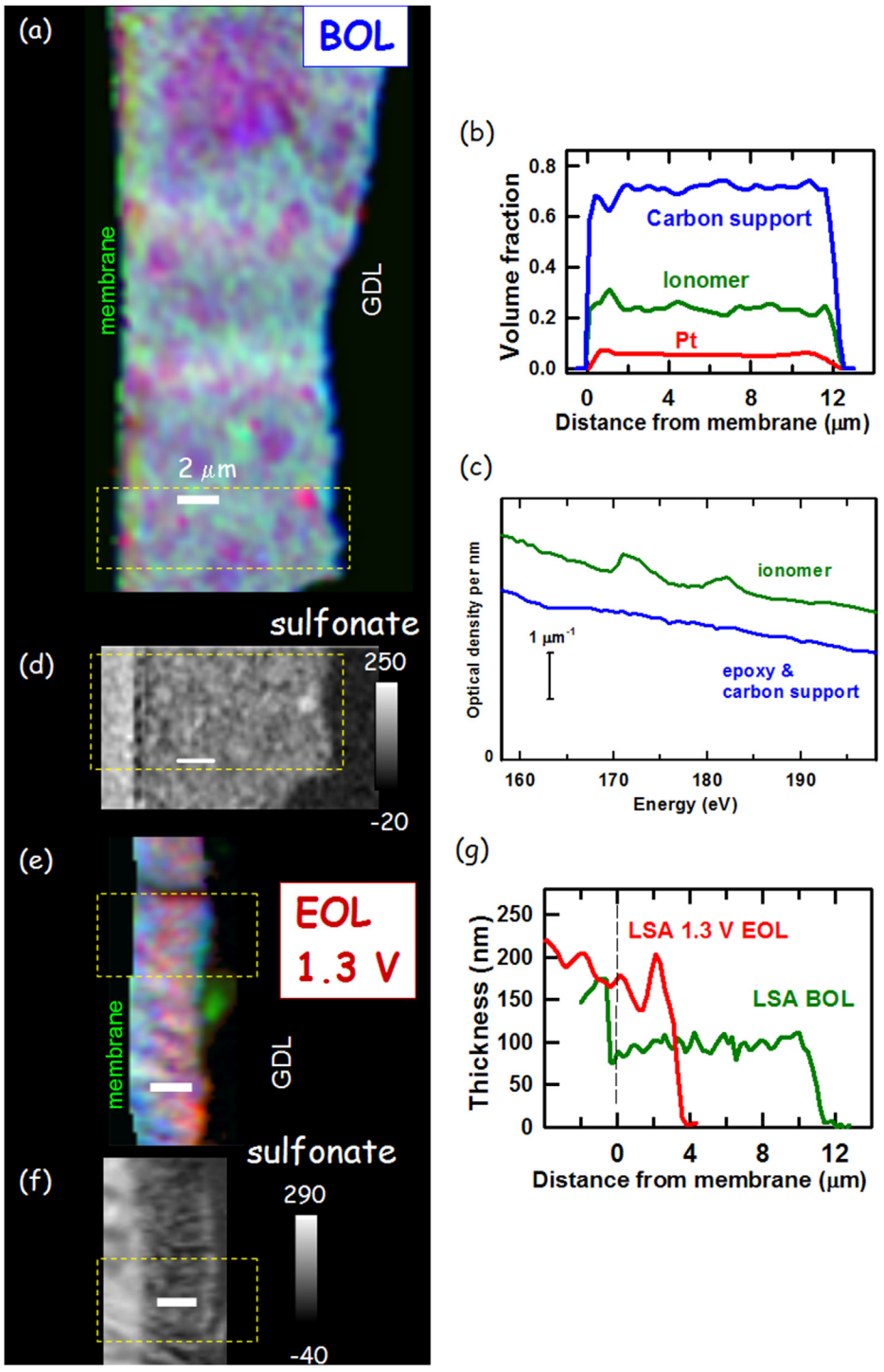

Fig. 13. (a) Color coded composite of the component maps of the LSAC BOT cathode derived from the C 1s and F 1s 4-energy approach (red – catalyst, green – ionomer, blue – carbon support). (b) Horizontal profiles of the volume fraction of the catalyst, ionomer and carbon support across the cathode taken from the same area from which the sulfonate signal was measured (yellow rectangle in (a)). (c) NEXAFS spectra in the S 2p region of the membrane of LSAC BOT and the epoxy/carbon support, on an OD1 intensity scale. (d) Map of the sulfonate signal in the cathode and membrane region of the LSAC BOT derived from a S 2p image sequence fit to the reference spectra in (c). (e) Color coded composite of the component maps of the cathode for the LSAC EOT 1.3 V, derived from the C 1s and F 1s 4-energy approach. (f) Map of the sulfonate signal in cathode and membrane region of the LSAC EOT 1.3 V, derived from a S 2p image sequence. (g) Horizontal profiles of the thickness (nm) of the sulfonate across the cathode and membrane extracted from the sulfonate maps in (d) and (f). The vertical dashed line is the position of the membrane-cathode boundary. The PFSA levels in the membrane determined from the S 2p analysis are quite similar to those determined from the F 1s analysis [CLS]. (For interpretation of the references to color in this figure legend, the reader is referred to the web version of this article.)

suggesting there may have been partial loss of the sulfonate groups, although the accuracy of quantitation of ionomer from the S 2p edge is less than that for quantitation of ionomer from the F 1s edge.

4. Discussion

STXM measurements at the C 1s, F 1s, and S 2p edges have been used to image and quantify the thickness and volume fractions of

the key components of the PEM-FC MEAs (carbon support, ionomer, sulfonate, and Pt), and the changes in these components as the material was subjected to accelerated testing protocols. We have systematically studied MEAs using two different types of carbon support, LSAC and MSAC, at different cathode potentials (upper potential limits (UPL) of 1.0, 1.2, 1.3 V). Performance results [29] showed that both Pt catalysts exhibit the same degradation signature of platinum dissolution and support corrosion. However there are some subtle differences in degradation rates. The LSAC catalyst is slightly more stable at UPL $\leq$ 1.3 V, but notably less stable than MSAC catalyst at UPL = 1.0 V. This difference is likely associated with the highly graphitized walls and amorphous center of the LSAC support versus the more dispersed graphitic areas observed for the MSAC support. In both types of carbon supports, severe carbon corrosion was found to occur at UPL > 1.3 V leading to a decrease in the cathode catalyst layer thickness. As measured by STXM, this decrease was found to be associated with a large increase in the ionomer volume fraction (see Figs. 9d and 12d). This suggests that the ionomer in the cathode is relatively unaffected by the carbon corrosion process and thus gets increasingly concentrated in the remaining catalyst layer. Furthermore, the S 2p analysis of the LSAC BOT and LSAC EOT 1.3 V samples (Fig. 13) indicates that a considerable amount of sulfonate groups is still present in the cathode, even after severe carbon corrosion, indicating there is at most only partial loss of sulfonate groups at high cathode potentials. These results are in agreement with an observed decrease in the catalyst layer porosity and reactant diffusivity, and an increase in catalyst layer ionic resistance which subsequently results in fuel cell performance degradation (results to be published later). The Pt depletion layer seen in the EOT samples, along with the formation of a Pt band in the membrane, indicates that the migration of the Pt species is predominantly at the catalyst–membrane interface. This depletion layer will further affect the catalyst performance as it changes the current distribution and thus ionic resistance within the catalyst layer. Overall, the STXM results have provided valuable visualizations and direct, quantitative maps that significantly enhance other methods used to follow PEM-FC degradation under accelerated stress testing.

Acknowledgments

This work was supported by a Collaborative Research and Development grant (CRD 395013-09) from NSERC (Canada) and the Canada Research Chairs Program (Hitchcock) (950-204424). STXM studies were carried out at beamline 10ID1 at the Canadian Light Source (CLS), which is supported by the Canada Foundation for Innovation (CFI), NSERC, Canadian Institutes of Health Research (CIHR), National Research Council (NRC), Western Diversification and the University of Saskatchewan; and at the STXM on beamline 5.3.2.2 at the Advanced Light Source (ALS), which is supported by the Director, Office of Energy Research, Office of Basic Energy Sciences, Materials Sciences Division of the U.S. Department of Energy, under Contract No. DE-AC02-05CH11231. We thank Dave Cullen (ORNL) for measuring the high resolution TEM images. We thank Drs. Jian Wang and Chithra Karunakaran for their expert support of the SM beamline and STXM at the CLS. We thank Dr. Tolek Tyliszczak and David Kilcoyne for their expert support of STXM instrumentation at the ALS. Additional support was provided under U.S. DOE contract DE-EE0000466.

Appendix A. Supplementary data

Supplementary data related to this article can be found at http://dx.doi.org/10.1016/j.jpowsour.2014.04.119.

References

[1] R. Borup, J. Meyers, B. Pivovar, Y.S. Kim, R. Mukundan, N. Garland, D. Myers, M. Wilson, F. Garzon, D. Wood, P. Zelenay, K. More, K. Stroh, T. Zawodzinski, J. Boncella, J.E. McGrath, M. Inaba, K. Miyatake, M. Hori, K. Ota, Z. Ogumi, S. Miyata, A. Nishikata, Z. Siroma, Y. Uchimoto, K. Yasuda, K.I. Kimijima, N. Iwashita, Chem. Rev. 107 (2007) 3904.
[2] W. Schmittinger, A. Vahidi, J. Power Sources 180 (2008) 1.
[3] K.J.J. Mayrhofer, J.C. Meier, S.J. Ashton, G.K.H. Wiberg, F. Kraus, M. Hanzlik, M. Arenz, Electrochem. Commun. 10 (2008) 1144.
[4] S. Zhang, X.-Z. Yuan, J. Ng, C. Hin, H. Wang, K.A. Friedrich, M. Schulze, J. Power Sources 194 (2009) 588.
[5] S.F. Burlatsky, M. Gummalla, V.V. Atrazhev, D.V. Dmitriev, N.Y. Kuzminyh, N.S. Erikhman, J. Electrochem. Soc. 158 (2011) B322.
[6] K. Hartl, M. Hanzlik, M. Arenz, Energy Environ. Sci. 4 (2011) 234.
[7] M. Howells, C. Jacobsen, T. Warwick, in: P.W. Hawkes, J.C.H. Spence (Eds.), Science of Microscopy, Springer, NY, 2007.
[8] H. Ade, A.P. Hitchcock, Polymer 49 (2008) 643.
[9] A.P. Hitchcock, in: G. Van Tendeloo, D.K. Van Dyck, S.J. Pennycook (Eds.), Handbook on Nanoscopy, vol. II, Wiley, 2012, pp. 745–791.
[10] D. Susac, V. Berejnov, A.P. Hitchcock, J. Stumper, ECS Trans. 41 (2011) 629.
[11] D. Susac, V. Berejnov, A.P. Hitchcock, J. Stumper, ECS Trans. 50 (2012) 405–413.
[12] V. Berejnov, D. Susac, J. Stümper, V. Lee, A.P. Hitchcock, in preparation.
[13] D. Bessarabov, A. Hitchcock, Membr. Technol. 6 (2009) 6.
[14] W. Chao, P. Fischer, T. Tyliszczak, S. Rekawa, E. Anderson, P. Naulleau, Opt. Express 20 (2012) 9777.
[15] D. Susac, J. Wang, Z. Martin, A.P. Hitchcock, J. Stumper, D. Bessarabov, ECS Trans. 33 (2010) 391.
[16] V. Berejnov, A.P. Hitchcock, D. Susac, J. Stumper, ECS Trans. 41 (2011) 395.
[17] V. Berejnov, Z. Martin, M.M. West, S. Kundu, D. Bessarabov, J. Stumper, D. Susac, A.P. Hitchcock, Phys. Chem. Chem. Phys. 14 (2012) 4835.
[18] V. Berejnov, D. Susac, J. Stumper, A.P. Hitchcock, ECS Trans. 50 (2012) 361–368.
[19] B. Bozzini, M.K. Abyaneh, M. Amati, A. Gianoncelli, L. Gregoratti, B. Kaulich, M. Kiskinova, Chem. Eur. J. 18 (2012) 10196.
[20] L.M. Croll, H.D.H. Stover, A.P. Hitchcock, Macromolecules 38 (2005) 2903.
[21] N. Reid, J.N. Beesly, in: A.M. Glauert (Ed.), Practical Methods in Electron Microscopy, Elsevier, Amsterdam, 1991, p. 234.
[22] K.V. Kaznatcheev, Ch. Karunakaran, U.D. Lanke, S.G. Urquhart, M. Obst, A.P. Hitchcock, Nucl. Inst. Methods A582 (2007) 96.
[23] T. Warwick, H. Ade, A.L.D. Kilcoyne, M. Kritscher, T. Tylisczcak, S. Fakra, A.P. Hitchcock, P. Hitchcock, H.A. Padmore, J. Synchrotron Radiat. 9 (2002) 254.
[24] A.L.D. Kilcoyne, T. Tyliszczak, W.F. Steele, S. Fakra, P. Hitchcock, K. Franck, E. Anderson, B. Harteneck, E.G. Rightor, G.E. Mitchell, A.P. Hitchcock, L. Yang, T. Warwick, H. Ade, J. Synchrotron Radiat. 10 (2003) 125.
[25] C. Jacobsen, S. Wirick, G. Flynn, C. Zimba, J. Microsc. 197 (2000) 173.
[26] A.P. Hitchcock, aXis2000 is written in Interactive Data Language (IDL), It is available free for non-commercial use, http://unicorn.mcmaster.ca/aXis2000.html.
[27] I.N. Koprinarov, A.P. Hitchcock, C.T. McCrory, R.F. Childs, J. Phys. Chem. B 106 (2002) 5358.
[28] B.L. Henke, E.M. Gullikson, J.C. Davis, Atomic Data Nucl. Data Tables 54 (1993) 181.
[29] S. Wessel, Report on DoE Project FC049, Development of Micro-structural Mitigation Strategies for PEM Fuel Cells: Morphological Simulations and Experimental Approaches, 2011.
[30] K.A. Mauritz, R.B. Moore, Chem. Rev. 104 (2004) 4535.